23. This work is based on observations with the National Aeronautics and Space Administration (NASA)–European Space Agency HST obtained at the Space Telescope Science Institute (STScI), which is operated by the Association of Universities for Research in Astronomy under NASA contract NAS5-26555. Support for this work was provided by NASA through grant numbers GO-5021.01-92A and GO-5624.01-93A from the STScI. We thank K. Jones for his assistance in reducing and analyzing the data, the STScI support staff for their work in implementing our program, and R. Williams, the STScI director, for allocating some of his director's discretionary time for our program. The HST project scientist, D. Leckrone, deserves special thanks for the support he provided during all aspects of the HST comet-Jupiter campaign. We are also thankful for support provided by the HST program scientist at NASA headquarters, E. Weiler. We acknowledge helpful conversations with A. J. Dessler and M. A. McGrath regarding the interpretation of the spectral outbursts. Finally, we thank all of our colleagues who participated in the HST comet-Jupiter campaign for making this experience fun, as well as enriching.

HST Imaging of Atmospheric Phenomena Created by the Impact of Comet Shoemaker-Levy 9

H. B. Hammel, R. F. Beebe, A. P. Ingersoll, G. S. Orton, J. R. Mills, A. A. Simon, P. Chodas, J. T. Clarke, E. De Jong, T. E. Dowling, J. Harrington, L. F. Huber, E. Karkoschka, C. M. Santori, A. Toigo, D. Yeomans, R. A. West

Hubble Space Telescope (HST) images reveal major atmospheric changes created by the collision of comet Shoemaker-Levy 9 with Jupiter. Plumes rose to 3000 kilometers with ejection velocities on the order of 10 kilometers second^{-1}; some plumes were visible in the shadow of Jupiter before rising into sunlight. During some impacts, the incoming bolide may have been detected. Impact times were on average about 8 minutes later than predicted. Atmospheric waves were seen with a wave front speed of 454 ± 20 meters second^{-1}. The HST images reveal impact site evolution and record the overall change in Jupiter's appearance as a result of the bombardment.

The collision of comet Shoemaker-Levy 9 with Jupiter provided an unprecedented opportunity to study the reaction of a thick planetary atmosphere to a rapid deposition of energy. Predictions ranged from no observable effects (*1*) to major atmospheric disturbances, including explosive plumes (*2*, *3*) and atmospheric waves (*4*, *5*). Our atmospheric imaging program received 39 Hubble Space Telescope (HST) orbits to use the Wide Field and Planetary Camera 2 (WFPC2) for observations of dynamical effects in Jupiter's atmosphere from the event. We scheduled most of the orbits for the week of impacts, reserving six orbits for pre-impact characterization and nine orbits for observations of post-impact evolution. We selected a set of key filters (Table 1) and cycled through them as often as possible (*6*, *7*). To our delight, many effects on Jupiter's atmosphere were detectable with HST.

H. B. Hammel, J. R. Mills, T. E. Dowling, J. Harrington, and C. M. Santori are in the Department of Earth, Atmospheric, and Planetary Sciences, Massachusetts Institute of Technology, Cambridge, MA 02139, USA. R. F. Beebe, A. A. Simon, and L. F. Huber are in the Astronomy Department, New Mexico State University, Las Cruces, NM 88003, USA. A. P. Ingersoll and A. Toigo are in the Division of Geology and Planetary Science, California Institute of Technology, Pasadena, CA 91125, USA. G. S. Orton, P. Chodas, E. De Jong, D. Yeomans, and R. A. West are at Jet Propulsion Laboratory, California Institute of Technology, Pasadena, CA 91109, USA. J. T. Clarke is in the Department of Atmospheric and Ocean Sciences, University of Michigan, Ann Arbor, MI 48109, USA. E. Karkoschka is at Lunar and Planetary Laboratory, University of Arizona, Tucson, AZ 85721, USA.

Impact Sites

We detected impact sites for 15 fragments; five fragments left no discernible disturbance. Figure 1 shows a series of projections of several fresh (less than 3 hours old) impact sites as they would appear to an observer directly overhead. Table 2 gives our measurements of latitudes and longitudes of the detected sites, along with the predicted impact times and locations (*8*). From the observed longitudes, we inferred impact times. We also classified each impact site by its apparent size in the first image after impact; these classes agree roughly with pre-impact fragment brightnesses (*9*).

For the largest fresh impact sites, we noted a consistent morphology: a prominent circular ring and sometimes a faint ring inside the main ring concentric with it but visible mainly on the northwest side of the ring center, a small triangle with its apex near the ring center and its base to the southeast, a larger crescent-shaped ejecta also to the southeast, and rays in the crescent that seemed to emanate from a point slightly to the southeast of the ring center. In the methane absorption band, impact debris was brighter than the normal jovian clouds, suggesting that it was at a relatively high altitude, above most of the methane gas. At other wavelengths, the impact debris appeared darker than the normal jovian clouds. We discuss here the asymmetric ejecta; waves are discussed in more detail below.

Ballistic ejecta pattern. The outer edge of the crescent formed by impact G (the G impact crescent) is 13,000 km from the ring center (which presumably marks the point of maximum energy release). The speed of the ejecta must have been at least 17 km s^{-1}, assuming ballistic particles launched at an elevation angle of 45° (the predicted elevation angle of both the bolide and the ejected plume). The crescent shape of the ejecta suggests that the range of elevation angles is small. Assuming this range was centered around 45°, the vertical component of the velocity is slightly greater than 12 km s^{-1}. At this speed, particles will travel for 17 min before returning to their initial ejection level, during which time they will rise to a height of 3200 km. The latter is close to the maximum height of the G plume determined from HST images, and this time is consistent with observed plume durations (Figs. 2 and 3) (Table 3). At any other elevation angle, the required velocity would be higher; for example, material ejected straight up at the same velocity of 17 km s^{-1} would reach 6400 km (higher than observed). The material is not highly collimated in azimuth: the crescent extends at least 180° around the impact site.

The azimuth of the symmetry axis of the ejecta pattern indicates how long the material was in flight, because the planet rotated during that time. The fragments entered the atmosphere at an elevation angle of 45°, with the azimuth angle 16° counterclockwise from south; models of oblique impacts (*3*) predict the ejection of material back along this same trajectory. To a good approximation, the vertical component of the rotation vector tells us how far the planet rotated while the material was in flight. The rotation increases the azimuth angle by $\Omega t \sin\phi$, where Ω is the angular velocity of the planet, t is the time of flight, and ϕ is the planetocentric latitude. For t = 17 min, corresponding to a height of 3200 km, the rotation angle is 7°, giving a total azimuth angle from south of 23°. However, the observed azimuth is 35° ± 5°, implying that the material was in flight for 45 min; this conclusion holds also for the material near the impact point, because the azimuth of the small triangle is at least 35°. Ejected material may slide along the top of the atmosphere following its oblique high-speed reentry. If friction with the underlying layer is low, the rotation is the same as if the

material were on a ballistic trajectory for 45 min. Clearly, further modeling is required for both the plumes and the subsequent ejecta pattern.

Rays in the ejecta and ejecta color. The rays appeared to emanate from a point 1000 to 2000 km southeast of the ring center (Fig. 1). This offset could have arisen either during the initial entry of the bolide or more likely during plume ejection and fallback. The bolide probably penetrated to a depth of a few hundred kilometers below the cloud tops, but because it entered at a 45° angle with respect to the vertical, the horizontal separation between the entry point and the point of deepest penetration is only a few hundred kilometers. On the other hand, the ejecta reached an altitude of 3200 km (Fig. 3). The intersection of the rays may refer to the center of collapse of this tall plume, rather than to the base of the plume. Alternatively, the linear features might not be rays, but instead could be arcs of material that were thrown out by irregular events during the ejection process. A comprehensive plume model is needed to address these issues. The color of the ring material appears to match that of the ejecta blanket (*10*), suggesting similar composition, but that says little about whether the material is cometary, jovian, or a mixture of the two. West *et al.* discuss this in more detail (*10*). In addition, Noll *et al.* (*11*) discuss the chemistry of the features derived from HST spectra, which give more information than color alone.

Table 1. Filters and exposure times. Exposure time and filter sequence varied in each orbit; for example, some orbits were specifically designated for ultraviolet imaging observations. Occasionally, we changed sequences because of circumstances in the HST orbit (for example, encroachment of the South Atlantic Anomaly). Here, λ is the wavelength and δλ is the bandpass; see Table 6.2 of the *WFPC2 Instrument Handbook* (*7*).

Filter name	λ (nm)	δλ (nm)	Exposure times (s) with camera	
			PC1	WF3
F218W	217.40	37.34	—	230, 260
F255W	260.90	42.17	300	40, 60
F336W	332.14	37.97	18	3, 3.5
F410M	409.04	14.65	10	2, 3
F547M	547.79	48.61	—	0.11, 0.16
F555W	539.84	123.16	0.3	—
FQCH4P15*	888.45	14.63	16, 30, 100	—
FQCH4N*	888.45	14.63	—	4, 10, 14
F953N	952.89	6.73	16, 35	8, 16

*P15 and N indicate the position of the partially rotated filter wheel for the methane quad filter (*7*).

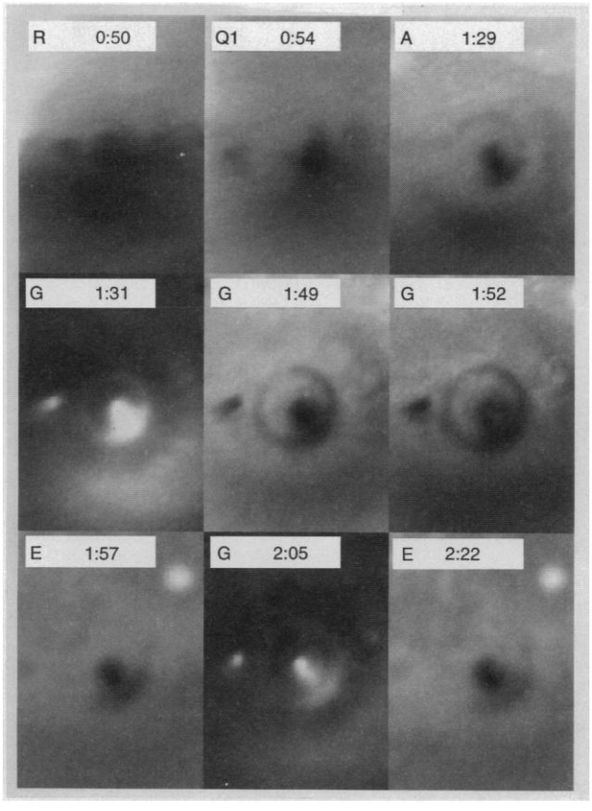

Fig. 1. Maps of five impact sites. These selected images of the A, E, G, Q1, and R impact sites are ordered by time from impact and show the outward expansion of atmospheric waves. Wave speed is independent of explosion energy. Also evident in the images is the impact-induced morphology: a dark central streak surrounded by a ballistic ejecta blanket with radial rays (for example, the G impact at 1:31). The rays do not point toward the center defined by the waves, but rather seem to emanate from a point 1000 km to the southeast. Any impactor large enough to create a wave also exhibited . asymmetric ejecta. Smaller impactors left only central disturbances (for example, in these frames, the Q2, N, and D sites are visible to the left of R, Q1, and G respectively). At continuum wavelengths, the features are dark; they are bright in the 889-nm methane-band images. Other sites undoubtedly had waves, but they were not sampled at the appropriate time by HST (waves were sought but not detected after 10 hours had elapsed since impact). In each frame, the letter in the upper left indicates the impact site and the number in the upper right is the time from impact in hours (Table 4). The wavelengths are as follows: top row, 336, 555, and 336 nm; middle row, 889, 555, and 336 nm; bottom row, 410, 889, and 336 nm. North is up; jovian west longitude increases to the left.

Plumes

On all four targeted events (A, E, G, and W), HST images detected plumes of ejected material above the limb of Jupiter (Fig. 2 and Table 3). The time scale from first detection to final settling into the upper atmosphere of Jupiter ranged from 15 to 20 min (Fig. 3). Because the fundamental optical properties of the plume phenomena were highly uncertain, we cycled through filters in order to maximize the probability of detecting a plume. Plume images later in the impact week were also used to study impact sites created earlier; this required complete filter coverage.

Initial plume images. Three unusual and provocative HST detections at the precise impact times of A, G, and W raised questions (Fig. 2). Were we somehow seeing the initial meteor flash, even though the bolide entered the atmosphere "over the horizon" as viewed from Earth and HST, or were we seeing ejected material rising above the horizon a minute or so later? A comparison of HST event times with those seen by the Galileo spacecraft and by ground-based observers proved useful in addressing these questions. We discuss impact G first, then impacts A and W.

After an evaluation of timing from different observations, we suspect we may have directly detected the initial bolide in an HST image of the G impact. The first G impact signal from the Galileo Photopolarimeter Radiometer (PPR) was at 7:33:32 universal time (UT) at a wavelength of 945 nm (*12*). The PPR signal resembled other PPR impact observations: a sharp rise (of a few seconds duration) interpreted as the initial meteor signal, followed by a 15- to 30-s decline presumably attributable to a decrease in temperature and an increase in plume size. The Galileo Near-Infrared Mapping Spectrometer (NIMS) also detected an event at 7:33:37 at several wavelengths between 700 nm and 5.3 μm (*13*).

We took an image at a wavelength of

889 nm (889-nm image) with HST from 7:33:16 to 7:33:46 UT (Table 3 and Fig. 2)—coincident with the Galileo bolide event—in which we clearly saw bright pixels in the shadow of Jupiter. PPR data indicate that the combined bolide-plume phase for G lasted for 50 s (*12*), during which the flux from the bolide-plume was 3% of the integrated jovian flux outside the methane bands; in the bands, it was closer to 15% of the integrated jovian flux. In the HST image, the flux was much less. It is unlikely that we saw impact debris rising above the limb in this first G image. As seen from HST, the impact occurred over the horizon. Material at the impact site would have to be 444 km above the 100-mbar limb to be visible from Earth. If the true limb is higher (for example, because the tangent ray is attenuated at a higher altitude), the altitude would be correspondingly greater. Refraction reduces this distance by only 45 km if the limb is at the 100-mbar level (*14*). Material would have to travel upward at 25 km s^{-1} to reach 400 km after 16 s (the maximum time between the G impact and the end of our image); material at this velocity would rise higher than that observed in later images.

Although it is possible that we detected the G bolide, we may also have seen light from the bolide scattering off the incoming cometary dust; HST images of fragments showed great extension of the nuclei along the path of motion (*15*). A third possibility is that bolide light reflected off dust left in the atmosphere by the breakup of the fragment upon entry. Regarding the first option, the jovian atmospheric pressure at 440 km above the 100-mbar surface is about 0.1 μbar (*16*), the same pressure at which meteor trails are seen in Earth's atmosphere (*17*); although only a small fraction of the total light from the bolide comes from this level, it may be enough to be detected from Earth. Similarly, in the second option, only a small fraction of the total light could be scattered to Earth by the incoming dust cloud, because the optical thickness of the dust cloud within a 1000-km radius around the fragments before the impacts was on the order of 10^{-6} (*15*). We may have seen a combination of these effects.

Bright pixels appeared in the first image in the A plume sequence (taken at 20:13:16) at the expected location of a plume (Table 3 and Fig. 2); near-infrared observations at Calar Alto, Spain, showed an initial event starting at 20:11:30 ± 5 s, continuing for about 30 s (*18*). However, observations of the wave generated by the A explosion put the impact event at 20:15:54 ± 30 s (formal error). In an image at 20:15:16, we saw nothing, but 3 min later we saw the clear signature of a rising plume. The bright pixels in the first image do not look like a cosmic ray strike, and we have ruled out background stars and jovian moons as causes for the anomalous first image. We suspect the timing derived from the wave may be incorrect; it is inferred from predicted times and longitudes and is really good to only within minutes, whereas the times of the HST plume images in Table 3 are accurate to within 0.5 s. If so, the first image may contain the incoming bolide (or associated phenomena), the second image was taken while it had disappeared behind the planet, and the third image captured the emerging plume 5 min later. Because the A impact occurred furthest around the limb from Earth, a long delay between impact and plume is more likely than for the other plumes we observed.

We may have made a similar detection in

Table 2. Summary of detected impacts: locations, times, and relative sizes.

Fragment*	Class†	Predictions‡			HST detection of impact§				Inferred impact time‖ (hh:mm:ss ± mm)
		dd:hh:mm:ss	Lat.	Lon.	Method	Lat.	Lon.	Frame	
A = 21	2a	16:19:59:42	−43.15	178	Wave	−43.41 ± 0.05	187.8 ± .03	—	20:15:54 ± 1
					Site	−43.54 ± 1.0	186.3 ± 2.0	0i04	20:13:24 ± 3
					Plume	—	—	0c01	20:13:16 ± 0.2
B = 20	3	17:02:54:15	−43.17	70	Site	−42.79 ± 1.0	71.1 ± 2.0	0g05	02:56:09 ± 3
C = 19	2a	17:07:02:15	−43.38	218	Site	−43.41 ± 1.0	225.0 ± 2.0	0i04	07:13:51 ± 3
D = 18	3	17:11:47:02	−43.46	30	Site	−43.29 ± 1.0	33.5 ± 2.0	0g05	11:52:50 ± 3
E = 17	2a	17:15:04:47	−43.48	149	Wave	−43.48 ± 0.05	153.5 ± 0.2	—	15:12:11 ± 1
					Site	−44.54 ± 1.0	153.5 ± 2.0	0i04	15:12:11 ± 3
G = 15	1	18:07:28:53	−43.60	23	Wave	−43.65 ± 0.04	25.7 ± 0.2	—	07:33:17 ± 1
					Site	−43.66 ± 1.0	26.8 ± 2.0	0p03	07:35:11 ± 3
					Plume	—	—	0o02	07:33:16 ± 0.5
H = 14	2a	18:19:26:03	−43.74	97	Site	−43.66 ± 1.0	101.4 ± 2.0	0v03	19:33:21 ± 3
K = 12	1	19:10:18:22	−43.80	275	Site	−43.29 ± 1.0	282.6 ± 2.0	1905	10:30:58 ± 3
L = 11	1	19:22:09:08	−43.92	344	Site	−42.79 ± 1.0	351.6 ± 2.0	6803	22:21:44 ± 3
N = 9	3	20:10:20:03	−44.30	66	Site	−43.41 ± 1.0	73.1 ± 2.0	1a03	10:30:09 ± 3
Q2 = 7b	3	20:19:47:19	−44.26	48	Site	−44.67 ± 1.0	47.5 ± 2.0	1a03	19:46:31 ± 3
Q1 = 7a	2b	20:20:04:48	−44.05	58	Wave	−44.37 ± 0.1	64.0 ± 0.5	—	20:14:42 ± 1
					Site	−43.41 ± 1.0	66.3 ± 2.0	1a03	20:18:24 ± 3
R = 6	2b	21:05:28:24	−44.07	39	Wave	−44.17 ± 0.1	46.8 ± 0.5	—	05:41:18 ± 1
					Site	−44.50 ± 1.0	43.6 ± 2.0	1a03	05:36:06 ± 3
S = 5	2c	21:15:12:46	−44.16	31	Site	−43.91 ± 1.0	34.0 ± 2.0	1l06	15:17:46 ± 3
W = 1	2c	22:08:00:52	−44.15	280	Site	−44.29 ± 1.0	284.8 ± 2.0	1o03	08:08:46 ± 3
					Plume	—	—	1n05	08:06:16 ± 0.1

*Impact sites for fragments F = 16, P2 = 8b, T = 4, U = 3, and V = 2 were not detected. Fragments J = 13, M = 10, and P1 = 8a were omitted because they faded from view (the letters I and O were not used). HST images in March 1994 showed that P2 = 8b and G = 15 had split, but there were insufficient data to obtain independent predictions for the subcomponents. †Classification of the sizes of the impact sites, based on the first view after impact. Class 1 (G, K, and L) = dark region >10,000 km, large ejecta, probably multiple waves; class 2a (A, C, E, and H) = 4000 < impact site < 8000 km, medium ejecta, possibly multiple waves; class 2b (R and Q1) = medium but slightly smaller ejecta, probably single wave; class 2c (S and W) = <6000 km, classification based on ground-based data, impacts occurred near earlier sites and are somewhat confused; class 3 (B, D, Q2, and N) = <3000 km, no ejecta, no wave; class 4 (F, P2, T, U, and V) = not detected, not shown in table. ‡Predictions from (*37*). The dynamical model used for the predictions includes perturbations that are a result of the sun, planets, Galilean satellites, and the oblateness of Jupiter. The planetary ephemeris used was DE245. The predicted time (dd:hh:mm:ss) is the time the impact would have been seen at Earth if the limb of Jupiter were not in the way. The date is the day in July 1994; the time is universal time. Latitudes are planetocentric (planetographic latitudes are about 3.84 degrees more negative). Longitudes are System III, measured westward on the planet. §Latitudes are planetocentric; longitudes are System III. "Frame" is the image used to measure latitude and longitude of impact site (the prefix "u2fi" has been deleted). Multiple images were used for wave measurements; the number of images used for A, E, G, Q1, and R are two, six, eight, one, and three, respectively. ‖Three methods were used for determining impact times: for "sites" and "waves," the time was obtained by taking the difference in longitude between HST measurements and the predictions and assuming a rotation period of 9.92492 hours (1.654153 min $degree^{-1}$); for "plumes," the time is that of first image showing brightening.

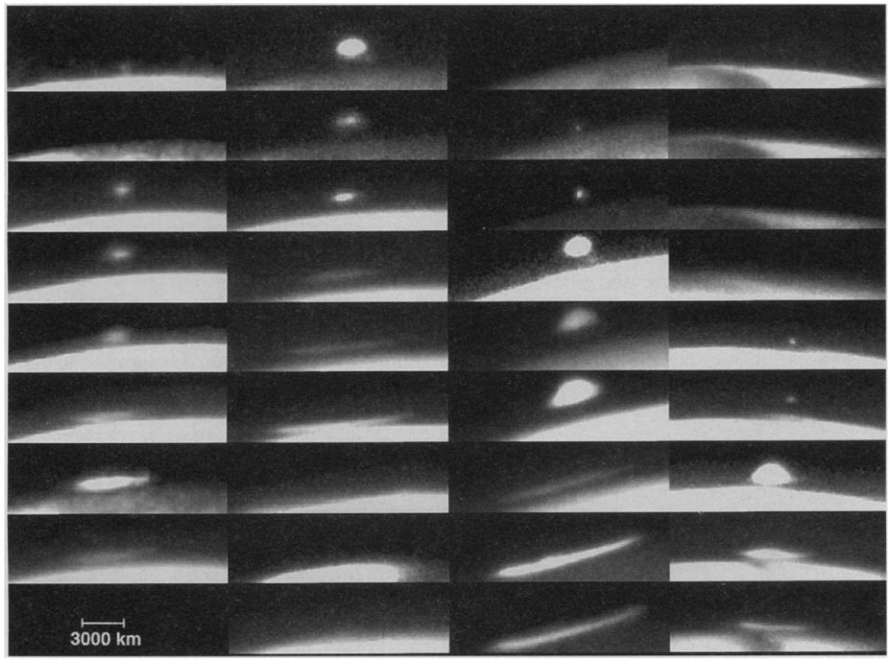

Fig. 2. Time sequences showing plumes from four impacts. From left to right, the columns show a series of images from A, E, G, and W, respectively. Table 3 gives times and filters; Fig. 3 shows plume heights versus time. Note in particular the simultaneous detection of thermal emission and reflected sunlight in the first E image and the fourth G image; the thermal emission clearly traces the entry path of the meteor (or the exit path of the rising plume). The seventh W image shows horizontal extension of reflected light (the structure on the disk in the W plume sequence is the site of the K impact, which occurred 3 days earlier). The apparent horizontal offset between the sixth and seventh W images is real and not a problem with navigation: we can navigate the images to better than half a pixel (*6, 22*). The A images have been scaled to match the other images. The position angle of north with respect to the vertical in the images is 133.5°, 133.7°, 126.0°, and 141.5° for A, E, G, and W, respectively.

the initial HST image of the W plume sequence (Table 3) (Fig. 2). We obtained a 555-nm image of the W plume at 08:06:16, within 0.5 s of a 559-nm image obtained by the Galileo Solid-State Imaging (SSI) experiment at 08:06:16.67 (*19*). The SSI image was second in a sequence of three images (each separated by 2⅓ s) where the first emission appears from the W impact. The rapid rise of the SSI signal has been interpreted as radiation emitted by the initial meteor, suggesting that the shadowed HST W signal is also the radiative signal of the bolide. For this impact, material would have to be 137 km above the 100-mbar surface to be visible from Earth (refraction reduces this distance by less than 25 km). To be visible to HST so shortly after impact, ejected material would have to rise with a velocity greater than that we infer from our later plume images. As before, we doubt that we imaged a rising plume here and suspect possibilities similar to those for G.

Initial plume brightnesses. We measured fluxes for the initial plume events of A, G, and W and estimated equivalent brightness temperatures by assuming a solid angle of either the box centered on the brightest pixel (2 pixels by 2 pixels) or the single brightest pixel. The plumes may be partially transparent; thus, their true kinetic temperatures may be higher. The first A impact signal (20:13:16 UT) covered 4 pixels and was easily detectable after the surrounding

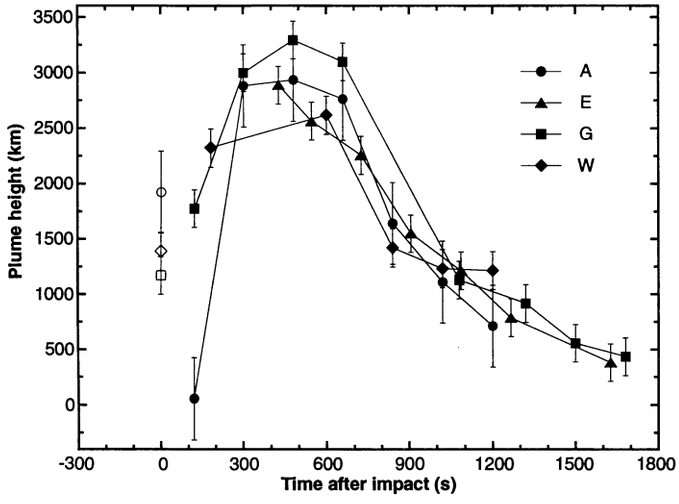

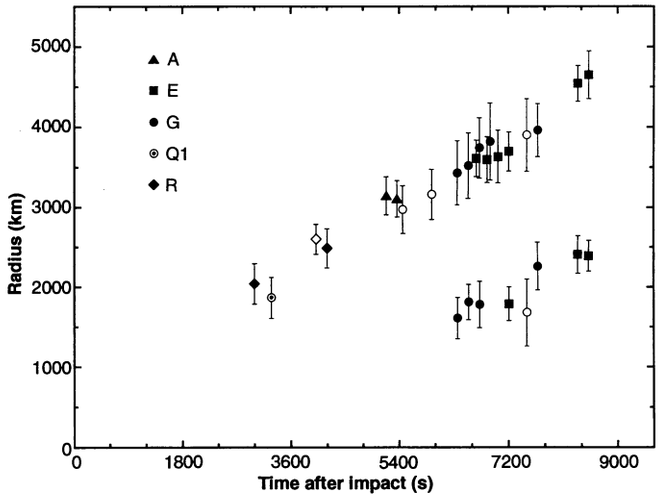

Fig. 3 (left). Plume height as a function of time. This figure shows the heights of the plume above the 100-mbar pressure level as a function of time after impact. The A and G plumes reached similar terminal altitudes, even though the sizes of the resulting impact sites varied by a factor of 2. The connecting lines are drawn in merely to aid the eye; the W plume probably attained a height comparable to that of the G and A plumes. The first points in the A, G, and W plume sequences (open points) are suspected to be related to the incoming bolide rather than to the rising plume and are defined as time 0; time 0 for E is from Table 2. Uncertainties in the measurements are on the order of 370 km for the A plume and 170 km for the other plumes. **Fig. 4 (right).** Propagation of impact-induced waves. Measurements of the positions of five main rings (upper cluster) and two secondary rings (lower cluster) are plotted as a function of elapsed time since impact (wave times are from Table 2). Open points are 889-nm methane-band images; see Table 4 for other wavelengths. The total length of the error bar represents the thickness of the ring. The best-fit line to the main ring observations does not cross through the origin, probably because of the sites' finite sizes at the time of wave creation. The slope of the line for the main ring is the wave propagation speed (454 ± 20 m s^{-1}). The slope of the inner ring is not well constrained, but probably lies between 180 and 350 m s^{-1}. Because the wave speed appears to be constant for impacts of varying sizes (G produced a much larger disturbance than A, for example), we infer that the propagation velocity is independent of explosion energy, which implies a linear wave.

planetary signal was subtracted. Its 889-nm flux is 3.5 (± 1.0) × 10^{-22} W cm^{-2} μm^{-1}, for a brightness temperature of about 516 ± 4 K (514 ± 4 K for the brightest pixel). In comparison, the 889-nm flux of the G event (7:33:16 UT) is 1.8 (± 0.2) × 10^{-18} W cm^{-2} μm^{-1} in a box 2 pixels by 2 pixels, equivalent to an average brightness temperature near 761 ± 4 K (714 ± 4 K for the brightest pixel).

The initial 555-nm flux of the W plume (08:06:16 UT) is 6.0 (± 1.0) × 10^{-17} W cm^{-2} μm^{-1}, equivalent to a brightness temperature over 1317 ± 12 K in a box 2 pixels by 2 pixels (near 1137 ± 12 K for the brightest pixel). Impact W may appear hotter than G and A because of a difference in geometry (W collided closer to the limb of Jupiter). As discussed above, our 555-nm W plume image was obtained within 1 s of a Galileo SSI 559-nm image, which recorded a flux orders of magnitude higher. The SSI filter is narrower (65 nm) than the HST filter (123 nm) and is included in the HST spectral region (*20*); therefore, much of the radiation detected by SSI but not by HST must have been emitted into the hemisphere not accessible to Earth-based telescopes.

Sunlit plume brightnesses. We also estimated the brightness of the sunlit plumes for several images; our findings (in watts $centimeter^{-2}$ $micrometer^{-1}$) were as follows: A plume, frame 0c04 at 20:21:16, 9.0 (± 1.0) × 10^{-17}; E plume, frame 0g02 at 15:21:16, 6.4 (± 0.6) × 10^{-21}; G plume, frame 0o06 at 07:44:16, 1.8 (± 0.2) × 10^{-14}; and W plume, frame 1n06 at 08:09:16, 1.62 (± 0.02) × 10^{-14}. These can be converted to *I/F* values (where *I* is intensity and πF is the solar flux) of 0.014 ± 0.002, 0.038 ± 0.004, 0.090 ± 0.01, and 0.042 ± 0.004 for A, E, G, and W, respectively, and indicate that the plume material was rather dark, as were the impact sites when they rotated into view.

A unique result from the HST plume imaging was the detection of bright pixels in the jovian shadow simultaneously with a plume top in reflected sunlight above the shadow, seen for the E and G impacts (Fig. 2). These pixels clearly show the angle of entry of the comet fragment or exit of the plume. Their brightness may be a result of thermal emission (if so, the brightness temperatures are on the order of 1300 to 1600 K), sunlight somehow scattered from the plume into the shadow, or a combination of both.

Plume geometry. Figure 3 shows estimated plume heights above the 100-mbar level (*21*, *22*). To our surprise, plumes for A and G seemed to reach nearly identical terminal altitudes of 3000 km, and we first detected plume E descending from nearly 3000 km. We have no information for W's peak plume height because of sparse temporal sampling, but its rise and fall indicate a similar height, a ground-based detection of the H plume also suggested a similar terminal altitude (*23*). Identical plume heights for explosions of different energies were not predicted (*2*, *3*) and have yet to be explained. The E impact seems to have a broader peak (shallower slope), whereas the W plume seems narrower; differing viewing geometry may be a factor. All four plumes observed by HST appeared to reach maximum height within 6 to 8 min of impact (Fig. 3) and were falling and spreading within 10 min of impact. All reached heights greater than 2400 km within 200 s, and A and G reached heights of nearly 3000 km within 300 s, which suggests a uniform vertical ejection velocity on the order of 10 to 12 km s^{-1}, independent of explosion energy.

The seventh image of the W sequence shows a peculiar unexplained feature; material can be seen in reflected sunlight extending northward beyond the edge of the well-defined plume top (Fig. 2). The material may be debris "splashing" outward, as predicted in some pre-impact models (*24*), and may be seen only in the W impact because of its position (closest to the jovian limb). The W plume is also intriguing because of its clear north-to-south asymmetry as the sequence progresses (Fig. 2). Our estimated error in the planet center is typically on the order of a few pixels, much smaller than the apparent shift in the plume

Table 3. Plume observations by HST. Frame prefix "u2fi" has been omitted. Filters differ for A because the observations were made with WF3 rather than with PC1. The universal times were measured on the following dates: A, 16 July; E, 17 July; G, 18 July; and W, 22 July. Exp., exposure time.

Frame	Filter	Exp. (s)	UT start	Description
			A	
0c01	FQCH4N	14	20:13:16	Emission in shadow from meteor?
0c02	FQCH4N	4	20:15:16	Nothing visible
0c03	F953N	16	20:18:16	Plume in sunlight
0c04	F547M	0.16	20:21:16	Plume spreading
0c05	F410M	2	20:24:16	Plume falling
0c06	F336W	3.5	20:27:16	Plume settled to disk
0c07	FQCH4N	4	20:30:16	Disk (better contrast)
0c08	F953N	16	20:33:16	Disk
			E	
0g01	FQCH4P15	30	15:19:16	Plume in sunlight, thermal tail
0g02	FQCH4P15	16	15:21:16	Larger plume
0g03	F953N	35	15:24:16	Plume falling
0g04	F555W	0.3	15:27:16	Plume settled to disk
0g05	F410M	10	15:30:16	Disk spreading
0g06	F336W	18	15:33:16	Disk stabilized
0g07	F255W	300	15:39:16	Dark disk?
0g08	FQCH4P15	30	15:49:16	Bright disk?
0g09	F953N	35	15:52:16	Nothing visible
			G	
0o01	FQCH4P15	100	07:30:16	Maybe brightening near limb?
0o02	FQCH4P15	30	07:33:16	Emission in shadow from meteor?
0o03	FQCH4P15	16	07:35:16	Emission in shadow
0o04	F953N	16	07:38:16	Plume in sunlight, thermal tail
0o05	F555W	0.3	07:41:16	Larger plume
0o06	F410M	10	07:44:16	Even larger plume, thermal tail?
0o07	F336W	18	07:51:16	Disk on limb
0o08	FQCH4P15	100	07:55:16	Slightly wider disk
0o09	FQCH4P15	30	07:58:16	Disk stabilized
			W	
1n01	FQCH4P15	100	07:55:16	Nothing visible
1n02	FQCH4P15	30	07:58:16	Nothing visible
1n03	FQCH4P15	16	08:00:16	Maybe faint "arc" near limb?
1n04	F953N	16	08:03:16	Nothing visible
1n05	F555W	0.3	08:06:16	Emission in shadow from meteor?
1n06	F410M	10	08:09:16	Plume in sunlight
1n07	F336W	18	08:16:16	Larger plume, streak at base
1n08	FQCH4P15	100	08:20:16	Thick disk
1n09	FQCH4P15	30	08:23:16	Disk flat on limb

with time. More subtle north-to-south asymmetry can be seen for the other plumes. Detailed models of the plume physics will be required to develop a comprehensive model of these and other plume observations.

Waves

In images taken within 3 hours of the larger impacts, we detected transient "rings" that are most likely caused by atmospheric waves (Fig. 1). The most dramatic example was the multiple ring system created by the large G fragment. The circularity of the rings suggests that they are waves; debris features are asymmetric.

Wave velocity. If the rings around the impact sites are linear waves, they should expand with a speed independent of impact energy. We measured the radii of the circular features using a geodesic mapping technique. We first converted the image into a latitude-longitude map (*25*) and then transformed that into a distance-angle map around the estimated center position using a numerical algorithm to integrate the paths of geodesic trajectories emanating from the center position, taking into account Jupiter's oblate-spherical geometry (*26*). This produced maps of the impact sites with distance along the abscissa and angle along the ordinate. In properly centered geodesic maps, circular waves appear as straight vertical lines; radial features appear as horizontal lines. If the estimated center was off, the lines varied sinusoidally; we then corrected the center to yield straight lines. This produced an accurate center for the ring. We repeated this process on each image that showed a ring and averaged the results for all images of a given impact site (Table 1). We also mapped the original data from the G impact using a Mercator projection (which locally preserves shapes) and measured the location of the rings on these maps. The results were similar to those found with the geodesic method.

In Fig. 4, we plot positions of the main rings from the A, E, G, Q1, and R impacts, as well as those of the inner rings from E and G (Table 4). For the main rings, a best-fit line yields a slope (that is, propagation velocity) of 454 ± 20 m s^{-1} and a radius of 586 ± 125 km at the time of impact. A positive initial radius could arise from either nonlinear (faster) initial propagation or from a finite source size. If we constrain the line through the origin, the velocity is 544 ± 7 m s^{-1} (formal error). The velocity of the inner rings is not well determined by the data but is probably in the range of 180 to 350 m s^{-1} (*27*).

Wave type. Candidate wave types are acoustic waves and inertia-gravity (IG) waves. The minimum acoustic wave speed (found at the temperature minimum near the 100-mbar level) is over 750 m s^{-1}, significantly greater than the measured speed; nonlinear effects only make an acoustic wave faster. Although IG waves come with any speed up to 900 m s^{-1}, recent numerical models suggested speeds of 400 m s^{-1} in the stratosphere (*5*), and speeds of tropospheric waves trapped in the putative jovian water cloud could range from 130 m s^{-1} up to 400 m s^{-1} (*4*, *28*). If the wave is interpreted as an IG wave with a velocity of 454 m s^{-1}, the corresponding radius of deformation (*29*) would be 1800 km.

Wave visibility. Regardless of wave type, it is not obvious why we should see the waves at all. They have the same relative methane-band brightness as the other impact-related features, so they are relatively high in the atmosphere: features that are bright in the methane filter are generally composed of small particles at or above the 380-mbar level (*10*). Perhaps the wave causes partial condensation of debris material as it moves though the stratosphere; this material would be the same as what we see in the dark core of the fresh impact and in the crescent-shaped ejecta. Either an upward displacement or a rarefaction could cause condensation by lowering the temperature.

More specifically, the impact-generated material might normally be transparent in the gaseous phase but was rendered visible by the chemistry that occurred in the explosion and ejection. (The material could be condensed material from the 2-bar pressure level combined with a small amount of cometary material, which erupted out as the observed plumes and then fell back into the stratosphere.) For example, if the leading edge of the waves is actually the inner edge of the asymmetric ejecta (in three G impact methane images the half-maximum intensity contour of the debris inner edge appeared to move at approximately the rate of the outer wave), this may represent a compressional heating: the material becomes transparent again. This would be followed by temporarily cooling below the material's condensation temperature during the expansive phase of the wave. Presumably, the waves are not visible after 3 hours because they have moved past the cometary debris. For this scenario to work, the debris material must have been close to the condensation point. Also, the wave speed would be higher than that inferred from Fig. 4, because the leading edge of the wave is at a larger radius than the sharp visible ring according to this hypothesis. Further modeling is needed to identify the precise nature of the waves.

Impact Site Evolution

The jovian wind field caused both short-term and long-term evolution of the impact-generated features. For reference, we measured the zonal wind field by tracking features in our images and found it essentially identical to the wind profile determined from Voyager data, with winds of 35, −10, and 30 m s^{-1} at planetocentric latitudes −39°, −45°, and −49°, respectively (*30*). [There was a significant change in the number and spacing of the small, white anticyclonic ovals centered near planetocentric latitude −38° (*31*), which should not be confused with comet-induced effects.] The impacts occurred at about latitude −43° (Table 2), but they created ex-

Table 4. Atmospheric wave observations: ring radii. In the frames, the prefix "u2fi" has been deleted.

Site	Frame	Filter	Time of exposure (dd:hh:mm:ss)	Time after impact (hh:mm)	Main ring (km)	Small ring (km)
A	5c05	F410M	16:21:42:17	1:26	3146	
A*	5c06	F336W	16:21:45:17	1:29*	3106	
E	0h03	F953N	17:17:03:17	1:51	3609	
E	0h04	F547M	17:17:06:17	1:54	3594	
E*	0h05	F410M	17:17:09:17	1:57*	3631	
E	0h06	F336W	17:17:12:17	2:00	3697	1788
E	0h0b	F547M	17:17:31:17	2:19	4543	2406
E*	0h0c	F336W	17:17:34:17	2:22*	4649	2391
G*	0p01	FQCH4P15	18:09:04:17	1:31*	2970	
G	0p02	FQCH4P15	18:09:12:17	1:39	3160	
G	0p03	F953N	18:09:19:17	1:46	3430	1610
G*	0p04	F555W	18:09:22:17	1:49*	3520	1810
G*	0p05	F336W	18:09:25:17	1:52*	3740	1780
G	0p06	F255W	18:09:28:17	1:55	3820	
G*	0p07	FQCH4P15	18:09:38:17	2:05*	3900	1680
G	0p08	F953N	18:09:41:17	2:08	3960	2260
Q1*	6807	F555W	20:21:09:17	0:54*	1864	
R*	1906	F336W	21:06:31:17	0:50*	2040	
R	1908	FQCH4P15	21:06:48:17	1:07	2600	
R	1909	F953N	21:06:51:17	1:10	2485	

*Shown in Fig. 1.

tended sources, and therefore gradients in the wind shear as a function of latitude would have spread the material. Meridional transport by vortex motion may also accelerate this process. At the impact latitude, the winds are weakly eastward and the ambient vorticity is cyclonic (clockwise), but the expected vorticity of a warm core of an impact structure would be anticyclonic. Both models (32) and observations of normal Jovian features (33) suggest that that configuration would be unstable: such a vortex breaks up after a few turnaround times. In general, this is what we observed: the cores (central 1000 km) broke up and material was dispersed by the ambient tropospheric winds.

H site evolution. Figure 5 shows a time sequence of the H impact site. The first frame (0w05 taken at 9:20:16 UT on 19 July 1994) shows H at 13.8 hours after impact. The feature has a morphology typical of a relatively fresh impact site: a dark central streak and asymmetric ejecta debris to the southeast. The second frame, 1c05, was taken at 9:35:16 UT on 21 July. After another 2 days, material drifted northward toward a small white oval (a typical jovian anticyclonic feature). The H site was unusual because its central dark streak developed lobes as it evolved, giving it a starlike appearance. The ejecta to the southeast of the impact had spread and thinned. Twenty-one hours later at 6:34:16 UT on 22 July, the northward-moving material had been entrained around a white oval, and the central impact site had developed a growing westward projection at planetocentric latitude $-43.9 \pm 5°$. The rest of the dark material sheared according to the local wind profile, indicating that some of the particles had settled into the tropospheric winds. In the last image of site H (taken on 24 August 1994, more than 5 weeks after impact), little remained of H except a few dark streaks east and south of the original impact site, and dark material entrained around the small white oval to the north. The streaked material extended in longitude from 63° to 111°. The longitude shift translated to velocities of ~ 10 m s^{-1} just north of the impact site (one-fifth of the measured tropospheric wind) and 0.25 to 0.5 m s^{-1} south of the site. The extent of the longitudinal dispersion of the dark material was similar to that seen for other well-isolated impact sites, such as E and K.

L site evolution. Impacts G, K, and L created the largest sites; we examine L images here as a case study. A complex pattern of ejecta from the L site can be seen in two pairs of images obtained on 23 July 1994 (Fig. 6). The overlying ejecta were dark in F410M images and bright against the absorbing background in the methane images. In general, both filters revealed similar structure, indicating that the material was high enough to be above much of the atmospheric absorption. The ejecta extended about 11° northward and 14° southward of the impact site. There was no evidence of relative motion between the two colors.

We took the first pair of images 4 days after the L impact (Table 1). During this interval, the east-west displacement based on the measured tropospheric winds should have been less than 18°, but the ejecta spanned as much as 35° in longitude. By measuring the edges of the ejecta and locating our measured impact site, we concluded that the debris "sensed" the ambient tropospheric wind field; however, there was an additional eastward translation that may have been a result of a horizontal component of the initial expansion. Assuming an average expansion velocity over the 4-day interval, one finds expansion rates of 30 m s^{-1} northward and about 40 m s^{-1} southward from our measured impact site. This dispersion is likely a result of a combination of the local zonal velocity with the effective radial expansion velocity of the impact-created debris.

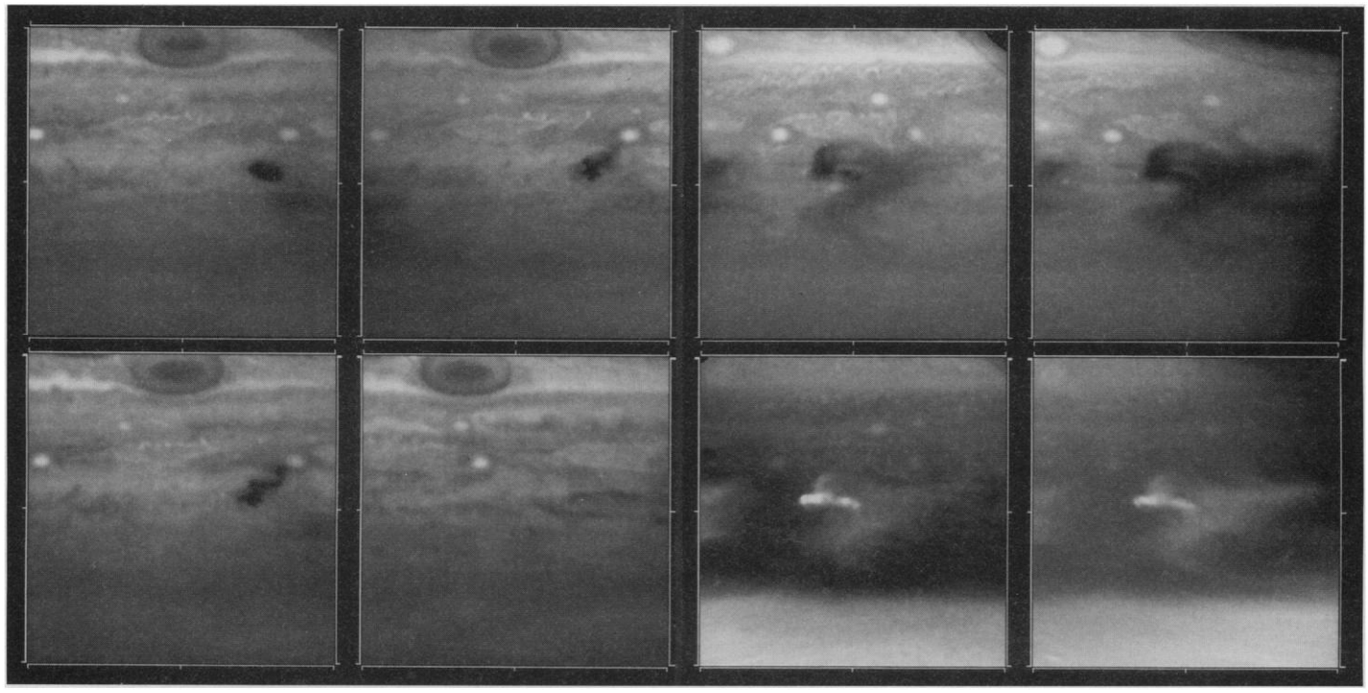

Fig. 5 (left, four panels). Temporal evolution of the H impact site. The maps are centered on planetocentric latitude −46.2° and System III longitude 115°, with a range in both latitude and longitude of ±30. All four images were taken through the F410M filter. The first frame (upper left) is about 14 hours after impact. The upper right frame was taken 2.5 days after impact, and the frame on the lower left was just 21 hours after that. The final frame at lower right was taken on 24 August 1994, more than a month after impact. **Fig. 6 (right**, four panels). The L impact site after 4 days. These images were obtained on 23 July 1994 in two orbits separated by 1.5 hours. In each orbit, a pair of images was taken through the 889-nm and 410-nm filters (1s01 and 1s05, and 1t01 and 1t05). The ejecta are dark in the blue wavelength images (upper pair) and bright against the absorbing background in the methane images (lower pair). Both filters in each pair reveal the same general structure. There is no evidence of relative motion between the two colors. The ejecta extend about 11° north and 14° south of the impact site. In the second pair, the feature is closer to the planetary limb, and material that is optically thin near the center of the disk becomes easily detectable as the site approaches the limb.

In the second pair of images, the feature was closer to the planetary limb, where the increase in solar incidence angle and emergent angle led to enhancement of structure in the ejecta and detection of a diffuse, low-contrast background; that is, material that was optically thin (nearly invisible) near the center of the disk became easily detectable as the site approached the limb. In the absence of aerosols, the 410-nm and the 889-nm filters generally were able to probe down to an atmospheric pressure level of 2.7 bar and 380 mbar, respectively, but observations near the limb moved the unit optical depth level to lower pressures (*10*). The optically thin material drifted northward with an average velocity of 30 m s^{-1}, consistent with the measurements of high-altitude material drift in ultraviolet images (*34*).

In general, the pattern and evolution of impact debris are consistent with a distribution of particles over a wide range of altitudes: a dense, central core created by the bolide and subsequent explosion, which may stretch over many scale heights down to the troposphere, and a surrounding thin blanket of dark material deposited at higher altitudes by the settling plumes. The rate of east-west expansion of the central core appears to be greater than that of the outlying region. For example, in a comparison of an L site methane image on 23 July (1s01) with one 32 days later (2108, obtained 24 August), the bright core had dispersed but structure in the outer diffuse region can be correlated with that in the earlier image, yielding velocities in the range of 0 to 3 m s^{-1} from latitudes from −30.5° to −56.6°. These velocities are consistent with a decrease in zonal wind with increasing altitude—for example, as was derived from the Voyager IRIS data (*35*): The relatively high outer ejecta are dispersed by the stratospheric winds and the lower core region is dispersed more effectively by stronger, tropospheric winds.

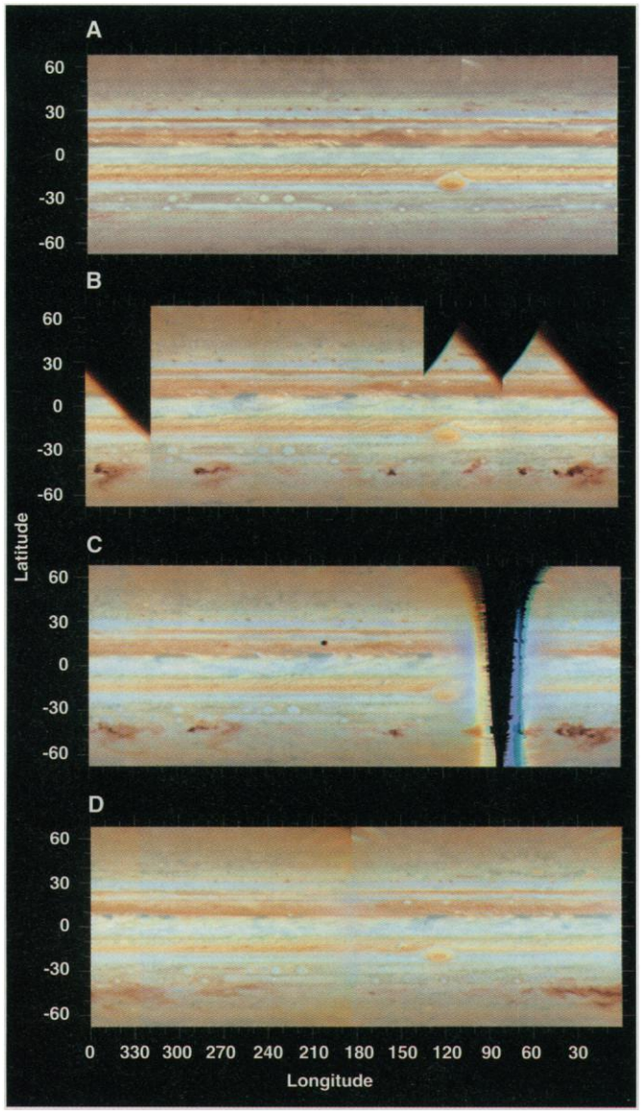

Fig. 7. Cylindrical map projections of Jupiter before and after the impact of comet Shoemaker-Levy 9. These cylindrical projections show the entire atmosphere of Jupiter in one map. Each map is created from at least five separate HST orbits. In each orbit, pictures were taken in red, green, and blue light. These were then recombined to approximate a true color as shown in the image. (**A**) The first map was taken on 15 July 1994, before the impacts began. This gives us a pre-impact base line. (**B**) The second map was taken on 23 July 1994, immediately after the impacts ended. Most of the impact sites are fresh, but one can begin to see evolution caused by the winds of Jupiter. (**C**) The third map was created with data obtained on 30 July 1994, a week after the impacts ended. Clear evolution is seen, particularly for material that is drifting southward from the impact sites. (**D**) The final map was taken on 24 August 1994. The material has continued to spread and thin, but there were still clearly localized sites of disturbance.

Overall jovian appearance. An overall perspective is shown in Fig. 7. These four maps show Jupiter before and after the impacts and demonstrate how the jovian winds have affected the features. The first map—taken on 15 July 1994—gave us a pre-impact baseline. We obtained the second map immediately after the impacts ended on 23 July. Most of the impact sites are fresh, but one can begin to see evolution caused by the winds of Jupiter. Most of the spread was zonal (that is, east-west), although there is evidence for meridional (north-south) spreading in high-resolution images. Because the fragments hit at a latitude where the winds are nonzero with respect to the rotation of the interior, they all appeared to drift in longitude. By a week after impact (30 July), clear evolution of the morphology was evident in the maps, particularly for material that had drifted southward from the impact sites. As the material drifted, it was caught up in the various eastward and westward jets. The shearing was consistent with the zonal winds.

A month after the impacts, on 24 August, we obtained the last images of the HST Comet Crash Campaign. The impact-created clouds were fading in contrast and spreading both in longitude and latitude, but there were still clearly localized sites of disturbance. The largest impacts—G, L, and K—retain demonstrably discrete structure in the 24 August map. The color of the features has not changed, suggesting that there have been no major chemical changes in the material since the features were created. Subtle changes in chemistry are probable. In a year, we may not see any remaining sign of these impacts, although the Galileo spacecraft may detect the last remnants of the major impact disturbances in well-targeted, high-resolution images. For Earth-bound observers, however, it appears that the main show was very short-lived on planetary timescales; we were fortunate to have had sufficient warning to prepare ourselves and our instrumentation to record the remarkable events on Jupiter in July 1994.

REFERENCES AND NOTES

1. P. Weissman, *Nature* **370**, 94 (1994).
2. K. Zahnle and M.-M. MacLow, *Icarus* **108**, 1 (1994).
3. M. B. Boslough, D. A. Crawford, A. C. Robinson, T. G. Trucano, *Geophys. Res. Lett.* **21**, 1555 (1994); T. J. Ahrens, T. Takata, J. D. O'Keefe, G. S. Orton, *ibid.*, p. 1087.
4. A. P. Ingersoll, H. Kanamori, T. E. Dowling, *ibid.*, p. 1083.
5. J. Harrington, R. P. LeBeau Jr., K. A. Backes, T. E. Dowling, *Nature* **368**, 525 (1994).
6. We used the WF3 detector of the Wide Field and Planetary Camera 2 for full-disk images; its 0.09953–arc sec pixels (*36*) corresponded to about 375 km at the sub-spacecraft point on Jupiter. For the higher resolution PC1 detector, the 0.0455–arc sec pixels (*36*) subtended about 170 km at the sub-spacecraft point. Significant vignetting in the 889-nm methane-band filter determined the image position in the PC

images (7). Rather than repoint the telescope several times in each orbit, we elected to retain the 889-nm pointing to maximize the number of images in each orbit. This constrained us to image only the southern half of Jupiter in PC sequences.
7. C. J. Burrows, Ed., *Wide Field and Planetary Camera 2 Instrument Handbook* (STScI publication, Baltimore, MD, May 1994).
8. For those impacts where we detected waves, we used the center of the wave to identify the latitude and longitude of the impact site. We also looked for a central impact (that is, we looked for ejecta and used the material's position to estimate the impact location) and then used a circle of 3 or 5 pixels to define a center in this region. In most cases, we examined "before," "after," and later images of the site to make sure we had the best location estimate. We inferred impact times from the difference between predicted and inferred longitudes.
9. H. Weaver *et al.*, *Science* **267**, 1282 (1995).
10. R. A. West *et al.*, *ibid.*, p. 1296.
11. K. S. Noll *et al.*, *ibid.*, p. 1307.
12. T. Martin and the Galileo PPR Team, personal communication.
13. R. Carlson and the Galileo NIMS Team, personal communication.
14. The refraction effect would be only 3 km if the limb were at the 10-mbar level. The reduction in height due to refraction is the bending angle of a ray passing tangentially through the atmosphere times the distance from the tangent point (the limb) to the impact point. This bending angle is $N(0)\ (2\pi R_J/H)^{1/2}$, where $N(0)$ is the atmospheric refractivity at the tangent point, R_J is the radius of Jupiter, and H is the scale height of the density distribution, assumed to be exponential (this formula is valid in the limit of a small bending angle and a small value for H/R_J). The refractivity of hydrogen is $1.4 \times 10^{-4}\ \rho/\rho(0)$, where ρ is the density and $\rho(0)$ is the density at standard conditions.
15. H. Weaver *et al.*, *Science* **263**, 787 (1994).
16. S. K. Atreya, *Atmospheres and Ionospheres of the Outer Planets and Their Satellites* (Springer-Verlag, New York, 1986).
17. V. I. Bronshten, *Physics of Meteoric Phenomena* (Reidel, Boston, 1983).
18. T. Herbst, D. P. Hamilton, H. Bohnhardt, J. L. Ortiz-Moreno, unpublished results.
19. C. Chapman and the Galileo SSI Team, personal communication.
20. M. Belton *et al.*, *Space Sci. Rev.* **60**, 413 (1992).
21. To find the plume heights, we first measured the x and y positions of the plume top and of the center of Jupiter (*22*). We then computed the distance from the plume top to the planet center and subtracted the distance from the planet center to the point on the limb below the impact. Finally, we added the vertical distance from the 100-mbar level of the impact site to the Earth line-of-sight for the longitude and time of the impact (for times, we used our estimates from Table 2). This rough calculation is good to within the errors of our ability to define the planet center and plume top.
22. We used programs originally developed for Voyager data reduction, which were subsequently modified for UNIX and IDL by C. Barnet.
23. J. Scotti *et al.*, poster presentation at the 26th Annual Division of Planetary Sciences Meeting, Washington, DC, 31 October–4 November 1994.
24. M.-M. MacLow and K. Zahnle, *Bull. Am. Astron. Soc.* **26**, 926 (1994).
25. We navigated all the images in a given HST orbit to determine an average planet center and used this average planet center to extract and remap the region around each impact site onto a 20° by 20° longitude-latitude map, with 20 pixels per degree (*22*). From this map, we estimated the circle's central longitude by averaging the circle's east and west extrema and estimated its latitude by averaging the north and south extrema.
26. The algorithm was developed by T. Dowling and C. Santori based on an outline from H. Goldstein, *Classical Mechanics* (Addison-Wesley, Reading, MA, ed. 2, 1980), pp.40–41.
27. For the inner ring, fixing the intercept at 586 km (that is, assuming the inner and outer rings started at the same time and radius) yielded a velocity of 189 ± 10 m s^{-1} (formal error), almost consistent with models suggesting a 3:1 ratio for the speeds of the two fastest modes (*28*) (*4*). Solving for both the slope and intercept implied a velocity of 353 ± 83 m s^{-1} with an intercept of −635 ± 613 km; in this model, the inner ring propagated almost as fast as the outer ring but began expansion roughly 30 min later. Finally, constraining the radius to 0 at time 0 implied a velocity of 268 ± 9 m s^{-1} (formal error). Because the correct physical interpretation of the inner wave is still unidentified, all of the above are plausible assumptions, and we simply state that the velocity of the inner ring is in the range of 180 to 350 m s^{-1}.
28. A. P. Ingersoll and H. Kanamori, unpublished results.
29. The radius of deformation, L_d, is a characteristic scale length in atmospheric dynamics and is defined as c/f, where c is the wave propagation velocity and f is the Coriolis parameter $2\Omega\sin\phi$, where Ω is the angular velocity of the planet and ϕ is the planetographic latitude.
30. A. P. Ingersoll *et al.*, *J. Geophys. Res.* **86**, 8733 (1981).
31. During the Voyager era, there were 13 ovals separated by about 25° longitude on average, with the maximum separation being 61°. If one assumed a missing oval, that implied a wave pattern with n = 14. The HST data show only seven ovals with longitudinal spacing ranging from 110° to 28°, with about 50° being most common. The eastward drift rate of the features has remained constant at about 0.6° per day.
32. T. E. Dowling and A. P. Ingersoll, *J. Atmos. Sci.* **46**, 3256 (1989); G. P. Williams and R. J. Wilson, *ibid.* **45**, 207 (1988); P. S. Marcus, *Nature* **331**, 693 (1988).
33. M.-M. MacLow and A. P. Ingersoll, *Icarus* **65**, 353 (1986).
34. J. Clarke *et al.*, *Science* **267**, 1302 (1995).
35. P. J. Gierasch, B. J. Conrath, J. A. Magalhães, *Icarus* **67**, 456 (1986).
36. J. A. Holtzman *et al.*, *Publ. Astron. Soc. Pac.*, in press.
37. P. W. Chodas and D. K. Yeomans, personal communication.
38. We gratefully acknowledge the staff and management at the Space Telescope Science Institute (STScI) for their fortitude during these unusually challenging observations; we note in particular the assistance of our Comet Science Team colleagues H. Weaver, M. McGrath, and K. Noll, and the heroic efforts of A. Storrs during planning and execution of the observations. We thank J. Trauger and members of the WFPC2 Team for the marvelous instrument, and we also thank our anonymous referees for insightful comments on the manuscript. H.B.H. thanks C. Barnet and L. Gesner for support with software acquisition and development. These observations were made with the NASA-ESA Hubble Space Telescope, with support provided through grant GO-5624.08-93A from STScI, which is operated by the Association of Universities for Research in Astronomy under NASA contract NAS5-26555.

Impact Debris Particles in Jupiter's Stratosphere

Robert A. West, Erich Karkoschka, A. James Friedson, Mark Seymour, Kevin H. Baines, Heidi B. Hammel

The aftermath of the impacts of periodic comet Shoemaker-Levy 9 on Jupiter was studied with the Wide Field Planetary Camera 2 on the Hubble Space Telescope. The impact debris particles may owe their dark brown color to organic material rich in sulfur and nitrogen. The total volume of aerosol 1 day after the last impact is equal to the volume of a sphere of radius 0.5 kilometer. In the optically thick core regions, the particle mean radius is between 0.15 and 0.3 micrometer, and the aerosol is spread over many scale heights, from approximately 1 millibar to 200 millibars of pressure or more. Particle coagulation can account for the evolution of particle radius and total optical depth during the month following the impacts.

Aerosol debris from the impacts of fragments of comet Shoemaker-Levy 9 can serve as a tracer to study the jovian stratospheric circulation, which has been inferred only indirectly from measurements of thermal contrast and solar radiative heating (*1*). Analogous studies of particles injected into the terrestrial stratosphere by volcanic eruptions have provided a wealth of data about the earth's atmosphere (*2*).

Aerosol debris particles are valuable tracers of the stratospheric wind field because their global distribution can be determined with high spatial resolution from a few images. We obtained images taken with the Wide Field Planetary Camera 2 (WFPC2) on the Hubble Space Telescope (HST). To learn as much as possible about the altitudes of the particles and about particle microphysical processes, especially the particle size that determines the loss rate from sedimentation, we imaged Jupiter at a variety of wavelengths (from 230 to 955 nm), and we scheduled exposures to provide coverage of emission angle as features rotated across the disk. The opacity provided by molecular scattering at ultraviolet (UV) wavelengths and by CH_4

R. A. West, K. H. Baines, and A. J. Friedson are with the Earth and Space Sciences Division, Jet Propulsion Laboratory, California Institute of Technology, Pasadena, CA 91109, USA. E. Karkoschka is with the Lunar and Planetary Laboratory, University of Arizona, Tucson, AZ 85721, USA. M. Seymour is with University College, London, UK, and the Earth and Space Sciences Division, Jet Propulsion Laboratory, California Institute of Technology, Pasadena, CA 91109, USA. H. B. Hammel is with the Department of Earth Atmosphere and Planetary Sciences, Massachusetts Institute of Technology, Cambridge, MA 02139, USA.